






 Cite this: *RSC Adv.*, 2026, 16, 18891

# MgO/NiCoFe<sub>2</sub>O<sub>4</sub> modified electrochemical sensor for simultaneous detection of ascorbic acid and levofloxacin

 Iram Gul Chandio,<sup>a</sup> Jameel Ahmed Baig, <sup>\*b</sup> Imam Bakhsh Solangi,<sup>\*c</sup> Huma Shaikh, <sup>a</sup> Latif Ullah Khan,<sup>d</sup> Sajjad Hussain,<sup>e</sup> Saima Perveen, <sup>a</sup> Faisal K. Algathami <sup>b</sup> and Nadeem Raza<sup>b</sup>

The current study aimed to synthesize and characterize magnesium oxide–bimetallic nickel cobalt ferrite nanohybrid (MgO/NiCoFe<sub>2</sub>O<sub>4</sub>-NH) for its application in the simultaneous electrochemical detection of ascorbic acid (AA) and levofloxacin (LEV). The NiCoFe<sub>2</sub>O<sub>4</sub>-NPs were synthesized using the sol–gel green method and fabricated with MgO. The synthesized materials were characterized using advanced analytical techniques. XRD confirmed single-phase spinel and cubic structures of NiCoFe<sub>2</sub>O<sub>4</sub>-NPs and MgO/NiCoFe<sub>2</sub>O<sub>4</sub>-NH with an average crystallite size of 6.5 nm and 11.4 nm, respectively. SEM and AFM revealed spherical/semi-spherical morphologies and extremely rough surfaces of MgO/NiCoFe<sub>2</sub>O<sub>4</sub>-NH, respectively. The average zeta potential and hydrodynamic size of MgO/NiCoFe<sub>2</sub>O<sub>4</sub>-NH were –32.5 mV and 33.6 nm respectively. XAFS demonstrate that the MgO/NiCoFe<sub>2</sub>O<sub>4</sub>-NH possesses a highly ordered spinel-like structure with strong M–O and M–M interactions. Further, MgO/NiCoFe<sub>2</sub>O<sub>4</sub>-NH/GCE was fabricated by drop-casting method and tested for the electrochemical detection of AA and LEV using differential pulse voltammetry (DPV) in a 0.1 M Britton–Robinson buffer (pH 7). The calibration plot was drawn for AA and LEV in the concentration range of 0.05–400 μM ( $R^2 = 0.996$ ) and 0.1–450 μM ( $R^2 = 0.995$ ), respectively. The LODs/LOQs of AA and LEV were determined to be 0.013/0.043 and 0.0091/0.03, respectively. The developed MgO/NiCoFe<sub>2</sub>O<sub>4</sub>-NH/GCE represents a stable and reliable electrochemical platform with strong potential for simultaneous detection of AA and LEV in real samples.

Received 17th January 2026

Accepted 25th March 2026

DOI: 10.1039/d6ra00424e

[rsc.li/rsc-advances](http://rsc.li/rsc-advances)

## 1 Introduction

Recently, pharmaceutical residues in environmental and food matrices have emerged as a significant public health concern rather than solely an ecological problem.<sup>1</sup> Recent studies report that traces of pharmaceuticals are detected in more than 50% of surface water worldwide, which affects human health and the ecosystem in the long term.<sup>2</sup> The residues of many common pharmaceuticals (analgesics, antibiotics, antiepileptics, and hormones) persist in the environment even at minute levels.<sup>3</sup> Though many old water treatment technologies efficiently work on removing bulk pollutants, these are not particularly made for

the elimination of trace-level micropollutants. Hence, continuous release of these waste products was found in aquatic systems.<sup>4</sup>

Besides this, pharmaceutical residues in food products, particularly milk, have attracted more attention due to the extensive use of antibiotics as therapeutic and prophylactic drugs in dairy animals. Milk from cows, buffalo, and cattle is one of the most commonly consumed foods worldwide, as it is the source of essential nutrients such as lipids, minerals, proteins, and vitamins.<sup>5</sup> Among these nutrients, ascorbic acid (AA), also known as vitamin C, is naturally present in small amounts in milk and plays a crucial role as an antioxidant, protecting both the milk components and human health.<sup>6</sup> On the other hand, pharmaceutical residues such as antibiotics, including levofloxacin (LEV), may also be present in milk due to their therapeutic and prophylactic use in dairy animals.<sup>7,8</sup> The occurrence of such drug residues in milk is a matter of concern because it not only affects consumer health but also expands antimicrobial resistance.<sup>9</sup> Therefore, simultaneous monitoring of beneficial biomolecules and hazardous pharmaceutical residues in both environmental and food matrices is crucial for integrated public health protection.

<sup>a</sup>National Centre of Excellence in Analytical Chemistry, University of Sindh, Jamshoro 76080, Pakistan

<sup>b</sup>Department of Chemistry, College of Science, Imam Mohammad Ibn Saud Islamic University (IMSIU), P.O. Box 90950, Riyadh 11623, Saudi Arabia. E-mail: JAMughal@imamu.edu.sa

<sup>c</sup>Dr M. A. Kazi Institute of Chemistry, University of Sindh, Jamshoro 76080, Pakistan. E-mail: imambux.solangi@usindh.edu.pk

<sup>d</sup>Synchrotron-light for Experimental Science and Applications in the Middle East (SESAME), P.O. Box 7, Allan, 19252, Jordan

<sup>e</sup>Department of Natural Sciences, The Begum Nusrat Bhutto Women University, Sukkur, Pakistan


The low quantities of these residues, structural variety, and interference from other co-existing molecules make it difficult to identify pharmaceutical and healthcare items in complex matrices like water. Unfortunately, conventional water treatment systems are not specifically made to eliminate such micropollutants that result in their constant release into aquatic systems. Traditional analytical techniques, such as spectrometry and chromatography, are useful but impractical for on-site applications because they need costly reagents, complex equipment, and time-consuming sample preparation.<sup>10,11</sup> Fortunately, the electrochemical sensing has found an emergent alternative for real-time monitoring applications due to its high sensitivity, low cost, portability, and rapid response.

The electrochemical performance of sensors intensely relies on the composition of the electrode surface. Studies showed that the spinel nickel cobalt ferrite nanoparticles (NiCoFe<sub>2</sub>O<sub>4</sub>-NPs) have attracted greater attention because they possess efficient magnetic properties, high redox, as well as catalytic activities.<sup>12</sup> However, in one previous study, it was reported that NiCoFe<sub>2</sub>O<sub>4</sub>-based electrochemical sensors frequently undergo nanoparticle agglomeration, possess limited electroactive surface area, and moderate electron-transfer kinetics, which restricts the applications of NiCoFe<sub>2</sub>O<sub>4</sub>-NPs in simultaneous multi-analyte detection effectively.<sup>13</sup>

To overcome these restrictions, a heterostructure can be developed by integrating any metal oxide (MO) to NiCoFe<sub>2</sub>O<sub>4</sub>-NPs to form MO/NiCoFe<sub>2</sub>O<sub>4</sub> nanohybrid. The integration of MO to NiCoFe<sub>2</sub>O<sub>4</sub>-NPs increases adsorption capability and surface basicity toward electroactive species. This integration also results in interfacial heterojunctions, which enable faster electron-transfer kinetics.<sup>14</sup> Furthermore, MOs act as a structural spacer which improves electroactive surface area, decreases agglomeration of nanoparticles, increases accessibility of catalytic site, and provides long-term stability compared to NiCoFe<sub>2</sub>O<sub>4</sub>-based sensors.

Nanotechnology enables the development of multifunctional nanohybrids with tailored physicochemical properties.<sup>15</sup> Additionally, green synthesis using plant extracts provides an environmentally gentle approach, which evades harmful reducing agents and improves biocompatibility and particle dispersion. Despite the numerous advantages of MO-integrated NiCoFe<sub>2</sub>O<sub>4</sub> nanohybrid, only a single study has been reported for the detection of heavy metals.<sup>16</sup> However, the MO-integrated NiCoFe<sub>2</sub>O<sub>4</sub> nanohybrid has not been systematically investigated for the simultaneous electrochemical sensing of AA and LEV in complex biological and environmental samples.

Therefore, the current study aims to design magnesium oxide functionalized nickel cobalt ferrite nanohybrid (MgO/NiCoFe<sub>2</sub>O<sub>4</sub>-NH) to overcome the limitations of previously reported single-component MgO or NiCoFe<sub>2</sub>O<sub>4</sub>-NPs electrochemical sensors. The integration of MgO with spinel NiCoFe<sub>2</sub>O<sub>4</sub>-NPs can create a synergistic heterostructure that facilitates faster electron-transfer kinetics, increases the electroactive surface area, and offers more accessible catalytic sites.

In this work, MgO/NiCoFe<sub>2</sub>O<sub>4</sub>-NH was synthesized *via* a green method and deposited onto a bare GCE to form MgO/

NiCoFe<sub>2</sub>O<sub>4</sub>-NH/GCE. The integration of MgO with NiCoFe<sub>2</sub>O<sub>4</sub> improves stability, redox behavior, and reactivity, which make it advantageous for simultaneous detection. The synthesized MgO/NiCoFe<sub>2</sub>O<sub>4</sub>-NH was characterized by several analytical techniques to reveal its structure, size, and morphology. The MgO/NiCoFe<sub>2</sub>O<sub>4</sub>-NH/GCE-based differential pulse voltammetry (MgO/NiCoFe<sub>2</sub>O<sub>4</sub>-NH/GCE/DPV) method was applied to detect AA and LEV simultaneously in blood, dairy milk, and wastewater samples. The proposed MgO/NiCoFe<sub>2</sub>O<sub>4</sub>-NH/GCE/DPV-based heterostructured platform demonstrates enhanced analytical performance compared to previously reported single-component MgO or NiCoFe<sub>2</sub>O<sub>4</sub>-based sensors, highlighting its potential for integrated environmental and food safety monitoring.

## 2 Experimental work

### 2.1 Chemicals and reagents

All chemicals used in the experiments were of analytical grade. These chemicals were used without any further purification. The details of suppliers are provided in the SI. Furthermore, deionized water (18.2 MΩ cm) was used throughout the experiments.

### 2.2 Green synthesis of NiCoFe<sub>2</sub>O<sub>4</sub>NPs

The fresh Babur (*Vachellia nilotica*) plant leaves were cleaned using deionized water. After drying, 30 g of leaves were mixed with 250 mL of deionized water at 80 °C for 3 hours. The resulting solution was filtered and used to synthesize NiCoFe<sub>2</sub>O<sub>4</sub>-NPs.

Nickel, cobalt, and iron nitrates were mixed in a molar ratio of 0.5:0.5:2 to preserve the stoichiometry of the spinel NiCoFe<sub>2</sub>O<sub>4</sub> structure. 200 mL of extract was added to the nitrate mixture. The resulting solution was stirred at 80 °C while maintaining a pH of 7 to 9. The phytochemicals present in the extract acted as capping and reducing agents, facilitating the formation of NiCoFe<sub>2</sub>O<sub>4</sub>-NPs and controlling their growth. After the reaction was complete, the product (NiCoFe<sub>2</sub>O<sub>4</sub>-NPs) was washed, dried, and stored for electrochemical studies. Reproducibility was tested through triplicate synthesis batches.<sup>17,18</sup>

### 2.3 Fabrication of MgO/NiCoFe<sub>2</sub>O<sub>4</sub> nanohybrid

The NiCoFe<sub>2</sub>O<sub>4</sub>-NPs powder sample (0.1 g) was dispersed in 50 mL of a 2 mM magnesium acetate solution for 2 hours, then filtered. The residues were kept at pH 12 in NaOH (0.1 M) overnight. After precipitation, the product was filtered, dried, and calcined at 400 °C for 2 hours.<sup>19</sup>

### 2.4 Modification of MgO/NiCoFe<sub>2</sub>O<sub>4</sub>-NH/GCE

The bare GCE surface was gently scraped with alumina paste and then washed with ethanol and deionized water. A suspension of MgO/NiCoFe<sub>2</sub>O<sub>4</sub>-NH in deionized water containing 0.5% Nafion was sonicated for 30 min.<sup>20</sup> A 10 μL aliquot was drop-cast onto the GCE surface and dried at room temperature.<sup>21</sup> The modified MgO/NiCoFe<sub>2</sub>O<sub>4</sub>-NH sensor was used to detect the AA and LEV using the MgO/NiCoFe<sub>2</sub>O<sub>4</sub>-NH/GCE/DPV method.



## 2.5 Instrumentation

Various instruments were employed to study the crystalline structure, size, morphology, and purity of synthesized nano-materials. The detailed instrumentation is provided in the SI.

## 2.6 Electrochemical analysis procedure

The electrochemical experiments were performed in a cell with a three-electrode system. The Ag/AgCl ( $2.0 \text{ mol L}^{-1}$ ), MgO/NiCoFe<sub>2</sub>O<sub>4</sub>-NH/GCE, and a Pt wire were used as the reference, working, and auxiliary electrodes, respectively. Under ideal circumstances, including a quiet time of 2 s, a sampling width of 0.02 s, a pulse period of 0.2 s, an amplitude of 50 mV, and a pH 7.0 phosphate buffer (PhB), DPV was utilized to quantitatively detect the analyte.

## 2.7 Sample preparation

The blood specimens were collected from volunteers with the help of trained personnel (hired from the dispensary of the University of Sindh, Jamshoro), after obtaining written consent and informing each subject verbally about the proposed study.

The proposed study is approved by the University of Sindh with the void number DRGS/1099. For biological validation, human blood samples (serum) were obtained from healthy volunteers through standard collection procedures. Serum separation was carried out by centrifugation, and the samples were diluted appropriately with phosphate buffer before analysis. Further, fresh milk samples (cow, buffalo, and cattle) were collected from local dairy farms and retail outlets. The samples were subjected to simple pretreatment. Similarly, the wastewater samples were collected from five distinct locations in Hyderabad and Jamshoro and subjected to pretreatment. After pretreatment, DPV was performed on the resulting samples to quantify the AA and LEV using the MgO/NiCoFe<sub>2</sub>O<sub>4</sub>-NH/GCE sensor.

# 3 Results and discussion

## 3.1 Characterization

An SEM image of synthesized NiCoFe<sub>2</sub>O<sub>4</sub>-NPs is shown in Fig. 1a, which exhibits spherical morphology of the agglomerated particles. Further, the fabrication of MgO to NiCoFe<sub>2</sub>O<sub>4</sub>-

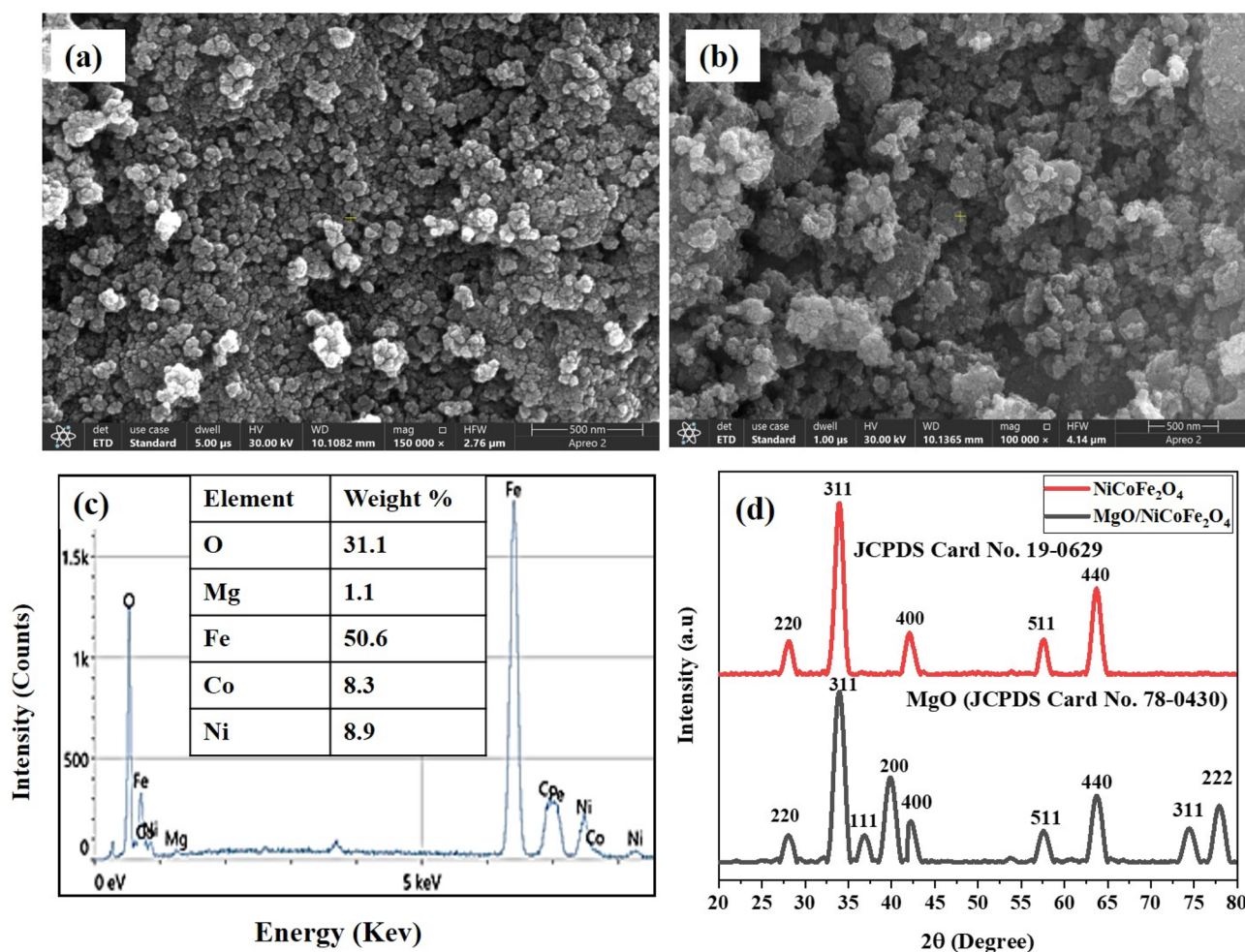


Fig. 1 SEM image of (a) NiCoFe<sub>2</sub>O<sub>4</sub>-NPs and (b) MgO/NiCoFe<sub>2</sub>O<sub>4</sub>-NH, (c) EDX spectrum of MgO/NiCoFe<sub>2</sub>O<sub>4</sub>-NH, and (d) XRD spectra of NiCoFe<sub>2</sub>O<sub>4</sub>-NPs and MgO/NiCoFe<sub>2</sub>O<sub>4</sub>-NH.



NPs revealed the change in morphology from spherical to semispherical (Fig. 1b). The results further showed a high agglomeration of MgO/NiCoFe<sub>2</sub>O<sub>4</sub>-NH, indicating the roughness of the surface of the synthesized materials.

The elemental composition of synthesized MgO/NiCoFe<sub>2</sub>O<sub>4</sub>-NH was studied by EDX, and the results are provided in Fig. 1c. The obtained spectrum showed the presence of Mg, O, Ni, Co, and Fe, which confirmed the successful synthesis of MgO/NiCoFe<sub>2</sub>O<sub>4</sub>-NH.

The XRD data is used to determine the crystal structure and to estimate the crystalline size of the NiCoFe<sub>2</sub>O<sub>4</sub>-NPs and MgO/NiCoFe<sub>2</sub>O<sub>4</sub>-NH (Fig. 1d). The XRD pattern of the synthesized NiCoFe<sub>2</sub>O<sub>4</sub> nanoparticles showed characteristic diffraction peaks at 2θ values corresponding to the Miller indices: (440), (220), (311), (400), and (511). The obtained diffraction patterns of synthesized materials matched well with the single-phase spinel structure with space group Fd3m (227) (JCPDS File No. 19-0629).<sup>22</sup> After fabrication with MgO, the XRD pattern of the MgO/NiCoFe<sub>2</sub>O<sub>4</sub>-NH exhibited additional peaks at: (111), (200), and (222). This suggests the successful incorporation or coating of MgO, which typically exhibits a cubic crystal structure. The

presence of both spinel ferrite and cubic MgO confirms the formation of a nanohybrid (MgO/NiCoFe<sub>2</sub>O<sub>4</sub>-NH) system. Furthermore, the sharp, well-defined peaks indicate good crystallinity of the synthesized NiCoFe<sub>2</sub>O<sub>4</sub>-NPs. The % crystallinity of the synthesized nanoparticles was 82%, and that of the MgO/NiCoFe<sub>2</sub>O<sub>4</sub>-NH was 86%.<sup>15</sup> The Debye-Scherrer equation was applied to determine the average crystallite size of synthesized NiCoFe<sub>2</sub>O<sub>4</sub>-NPs and MgO/NiCoFe<sub>2</sub>O<sub>4</sub>-NH, and the average crystallite size was found to be 6.5 and 11.4 nm.<sup>23</sup>

Further, the AFM method was used to analyze the topography and surface particle size distribution of MgO/NiCoFe<sub>2</sub>O<sub>4</sub>-NH (Fig. 2a), and the resultant data showed the extremely rough surfaces.<sup>24</sup> The results showed that the average surface particle size of MgO/NiCoFe<sub>2</sub>O<sub>4</sub>-NH was 3.5 nm, with a range of 1.2 to 4.01 nm (Fig. 2b). Additionally, the stable nature of the synthesized MgO/NiCoFe<sub>2</sub>O<sub>4</sub>-NH is supported by its surface charge and limited hydrodynamic diameter in dispersion. The surface charge of synthesized MgO/NiCoFe<sub>2</sub>O<sub>4</sub>-NH was analyzed by a zeta potential analyzer, and the average surface charge of synthesized MgO/NiCoFe<sub>2</sub>O<sub>4</sub>-NH was -32.5 mV (Fig. 2c). The size of synthesized MgO/NiCoFe<sub>2</sub>O<sub>4</sub>-NH was analyzed, and the

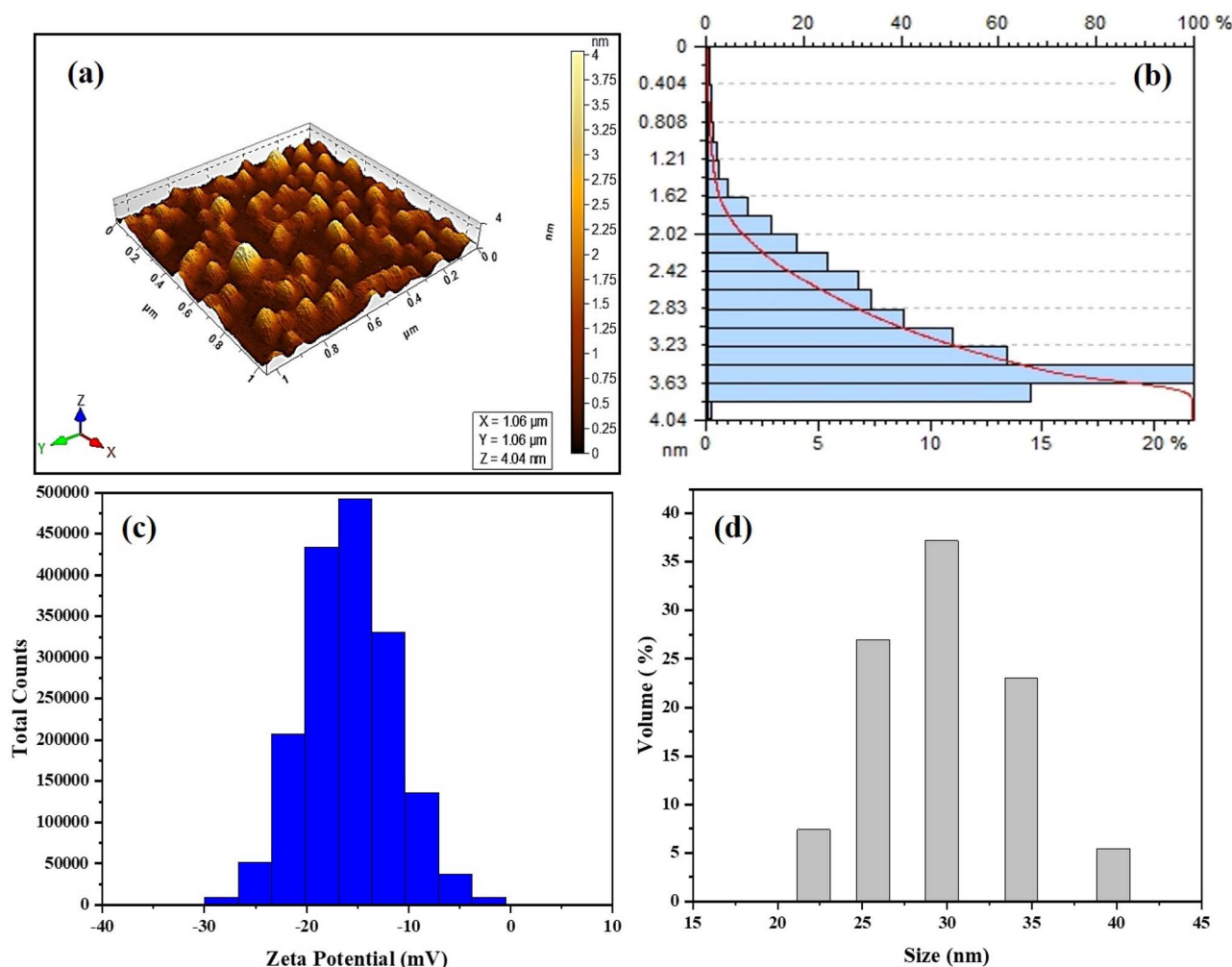


Fig. 2 (a) 3D topography, (b) AFM bar graph, (c) zeta potential, and (d) zeta size analysis of MgO/NiCoFe<sub>2</sub>O<sub>4</sub>-NH.



average zeta size (hydrodynamic diameter in dispersion) was 33.6 nm (Fig. 2d).

Further, it was noted that the obtained particle size differs across techniques. The apparent discrepancy in particle size between XRD (11.4 nm), AFM (3.5 nm), and zeta size (33.6 nm) arises from the different physical principles underlying these techniques. XRD provides the crystalline domain size, AFM measures particle height on a substrate (which may be underestimated due to tip effects and surface deformation), and zeta size reports the hydrodynamic diameter in suspension, including solvation layers and possible aggregation.

The X-ray Absorption Fine Structure (XAFS) analysis was employed to investigate the local atomic structure and oxidation states of the transition metals in the  $\text{MgO/NiCoFe}_2\text{O}_4\text{-NH}$ . In Fig. 3a, the XANES spectrum at the Co K-edge shows a distinct absorption edge at 7730 eV, which aligns closely with the edge position of a cobalt foil, suggesting that Co is present predominantly in oxidized states ( $\text{Co}^{2+}/\text{Co}^{3+}$ ), consistent with the  $\text{NiCoFe}_2\text{O}_4$  spinel structure. Fig. 3(b top), presents the corresponding EXAFS spectrum as a function of the wave vector  $k$ , plotted as  $k^2\chi(k)$ . The spectrum shows clear oscillatory behavior and good linearity, indicating a well-ordered local structure

around the cobalt atoms. Fig. 3(b bottom), displays the Fourier-transformed EXAFS data, with the x-axis representing the radial distance ( $R$ , Å). A prominent peak at approximately 1.5 Å corresponds to Co–O bonding, indicating metal–oxygen coordination in the first coordination shell. A second peak at approximately 2.8 Å is assigned to Co–Fe/Co–Ni interactions, supporting the formation of a mixed-metal spinel lattice.

In Fig. 3c, the Fe K-edge XANES spectrum reveals an absorption edge at approximately 7130 eV for the NH, which is close to that of the Fe foil, again indicating a relatively low oxidation state of iron in the NH. The XANES spectra at the Co and Fe K-edges were reinterpreted in light of standard spinel ferrite chemistry. Although the absorption edge positions appear close to metal foils, the entire spectral features and EXAFS fitting confirm that Co and Fe exist predominantly in oxidized states ( $\text{Co}^{2+}/\text{Co}^{3+}$  and  $\text{Fe}^{3+}$ ) within the  $\text{NiCoFe}_2\text{O}_4$  spinel lattice rather than in metallic form. This study aligns the XAFS analysis with the expected crystal chemistry of spinel ferrites and relevant literature. This confirms the successful incorporation of Fe into the spinel structure without significant oxidation. Fig. 3d provides a comparative analysis of the EXAFS radial distribution functions at the K-edges of Fe, Ni, and Co,

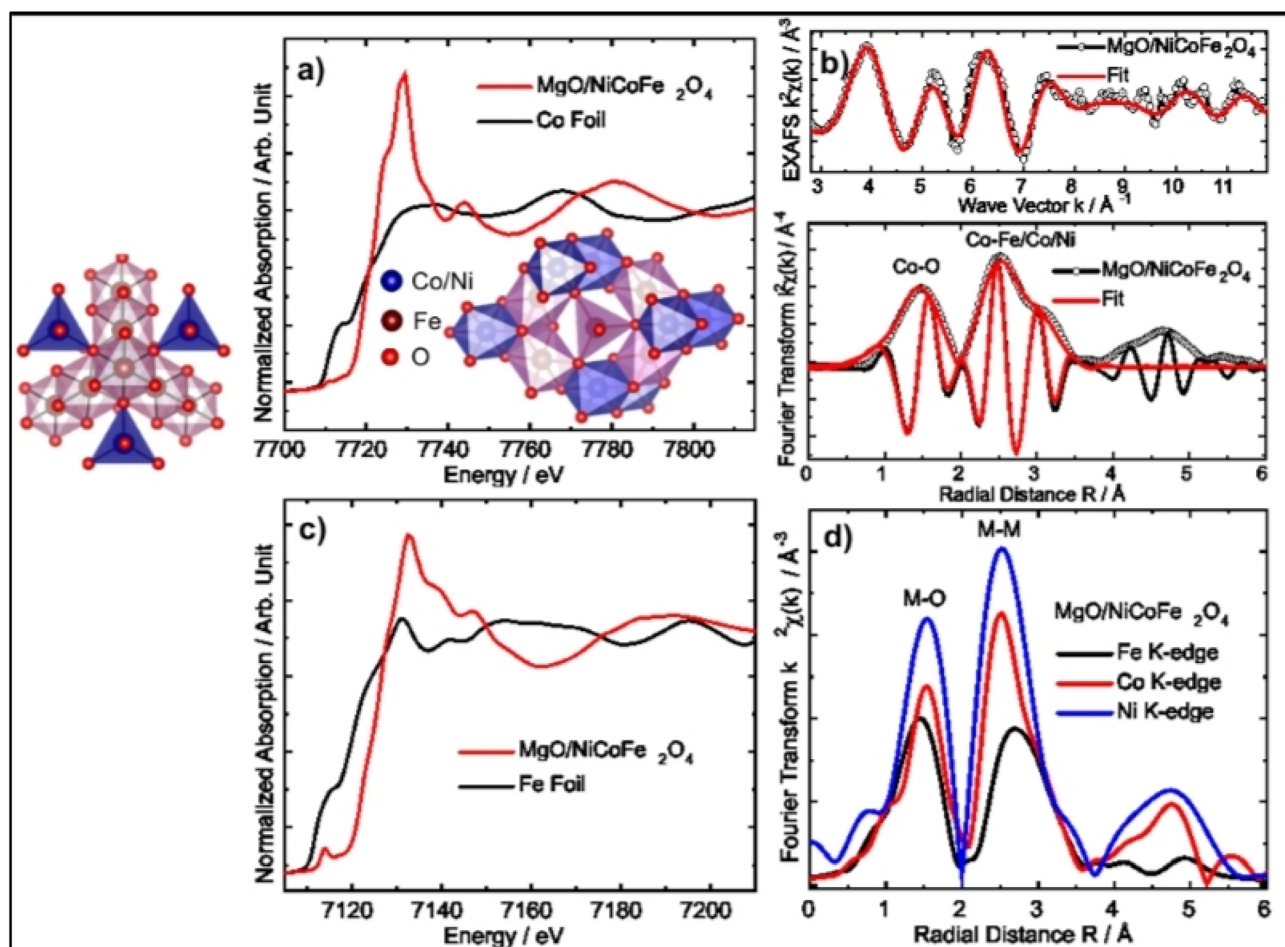


Fig. 3 XANES spectra of  $\text{MgO/NiCoFe}_2\text{O}_4\text{-NH}$  containing (a) Co K-edge, (b) its data, (c) Fe K-edge, and (d) comparative analysis of the EXAFS radial distribution functions.



plotted as  $k^2\chi(k)$  versus  $R$ . All three metal edges show strong M–O peaks around 1.5 Å, which indicates consistent oxygen coordination for all metal centres. It was noted that the Ni K-edge exhibits the highest  $k^2\chi(k)$  amplitude, suggesting a more pronounced local order or stronger backscattering at the Ni site. Peaks corresponding to M–M interactions are observed at approximately 2.5 Å, consistent with the spinel framework and confirming the presence of Fe–Ni, Fe–Co, and Co–Ni bonds in the second coordination shell. The XAFS data collectively demonstrate that the MgO/NiCoFe<sub>2</sub>O<sub>4</sub> NH holds a highly ordered spinel-like structure with strong M–O and M–M interactions, thereby confirming the successful synthesis and structural integrity of the MgO/NiCoFe<sub>2</sub>O<sub>4</sub>-NH.<sup>25</sup>

### 3.2 Electrochemical characterization of MgO/NiCoFe<sub>2</sub>O<sub>4</sub>-NH/GCE

The redox behaviour of bare and modified MgO/NiCoFe<sub>2</sub>O<sub>4</sub>-NH/GCE was studied, and it was observed that the modified GCE showed a greater current response than the bare GCE (Fig. 4a). The modified MgO/NiCoFe<sub>2</sub>O<sub>4</sub>-NH/GCE was selected for further study. Similarly, the electron transfer behavior of the modified

MgO/NiCoFe<sub>2</sub>O<sub>4</sub>-NH/GCE was also evaluated by the CV (Fig. 4b). A smaller difference was observed between the cathodic and anodic peak potentials at higher current intensities, indicating a higher electron-transfer rate, consistent with the larger active surface area of the electrode. By increasing the scan rate from 10 to 100 mV s<sup>-1</sup>, the redox currents are proportional to the square root of the scan rate, and a linear relationship was observed, indicating the diffusion-controlled behaviour of the electrode (Fig. 4c).

### 3.3 Electrochemical detection of ascorbic acid and levofloxacin

The electrochemical reduction and oxidation current responses of 250 μM AA and 250 μM LEV, respectively, were studied at a bare GCE and at MgO/NiCoFe<sub>2</sub>O<sub>4</sub>-NH/GCE in 0.1 M BRB (pH 7.0) using the developed method. The resulting data showed a pronounced electrochemical response of MgO/NiCoFe<sub>2</sub>O<sub>4</sub>-NH/GCE relative to GCE, confirming the excellent electrocatalytic potential of MgO/NiCoFe<sub>2</sub>O<sub>4</sub>-NH/GCE for the reduction and oxidation of AA and LEV, respectively (Fig. 5a).

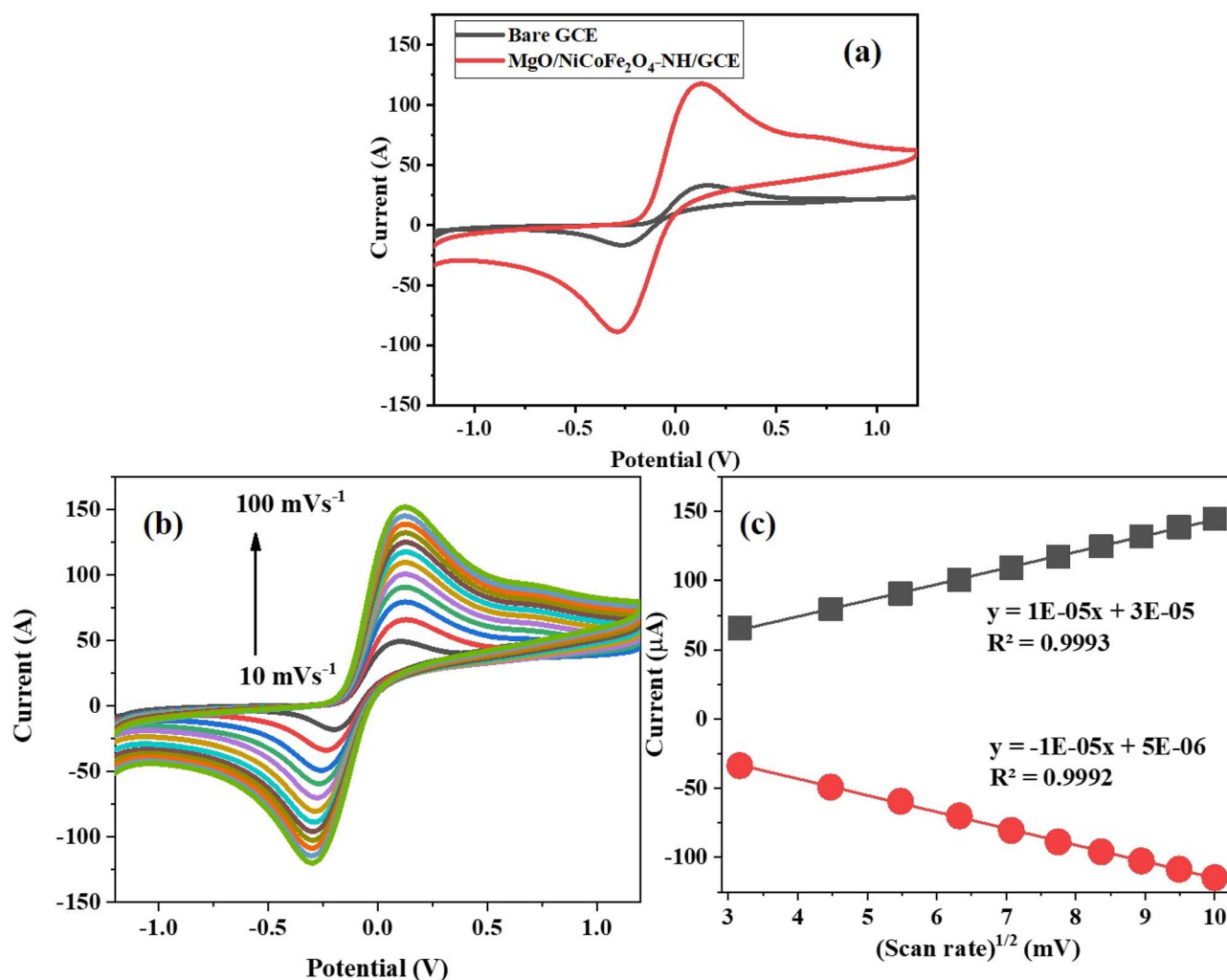


Fig. 4 (a) Redox behaviour, (b) scan rate, and (c) linear relationship analysis of MgO/NiCoFe<sub>2</sub>O<sub>4</sub>-NH/GCE.



The optimization of electrolytes was carried out by analyzing 250  $\mu\text{M}$  AA and LEV in Britton–Robinson (pH 7), acetate (pH 5), and phosphate (pH 7) solutions using the developed MgO/NiCoFe<sub>2</sub>O<sub>4</sub>-NH, as observed in zeta potential studies. Similarly, AA, a weak acid with a  $\text{pK}_a$  of around 4.1, is predominantly present in its deprotonated, anionic form at physiological pH. At lower pH, the protonated form of AA may interact more favorably with the electrode surface, whereas the optimal response at pH 7 suggests a balance between the ionization state of AA and the surface charge of the nanohybrid-modified electrode, thereby enabling efficient electron transfer. Thus, pH 7 provides optimal conditions for the simultaneous electrochemical detection of both analytes. Therefore, pH 7 of 0.1 M BR electrolyte was selected for further experiments. Moreover, a linear relationship was observed between varying pH and peak potential and the plot (Fig. 5d) gives a linear regression equation which is  $E_p = -0.0431x + 0.2215$  ( $R^2 = 0.988$ ) and  $E_p = -0.045x + 1.18$  ( $R^2 = 0.985$ ) for AA and LEV respectively. The linear shift of peak potential with pH for AA is  $E_p = -0.0431 \text{ pH} + 0.2215$  ( $R^2 = 0.988$ ) and for LEV is  $E_p =$

The pH of the solution plays a significant role in the electrocatalytic properties of sensors.<sup>26</sup> The pH was optimized from 4.0 to 8.0 of the BR electrolyte for the detection of AA and LEV using the developed MgO/NiCoFe<sub>2</sub>O<sub>4</sub>-NH/GCE/DPV method. The outcomes of the study showed that the maximum current response was observed at pH 7 (Fig. 5c). These variations in the peak currents appear to be connected to the  $\text{pK}_a$  values of LEV, which are 5.8 and 8.0.<sup>27,28</sup> Therefore, the LEV will adopt a positive charge under acidic conditions, exist as a zwitterion at pH values between 5.8 and 8.0, and become negatively charged at pH values higher than 8.0. The peak

current for the negatively charged LEV is significantly lower, and this may be related to the negative surface of MgO/NiCoFe<sub>2</sub>O<sub>4</sub>-NH, as observed in zeta potential studies. Similarly, AA, a weak acid with a  $\text{pK}_a$  of around 4.1, is predominantly present in its deprotonated, anionic form at physiological pH. At lower pH, the protonated form of AA may interact more favorably with the electrode surface, whereas the optimal response at pH 7 suggests a balance between the ionization state of AA and the surface charge of the nanohybrid-modified electrode, thereby enabling efficient electron transfer. Thus, pH 7 provides optimal conditions for the simultaneous electrochemical detection of both analytes. Therefore, pH 7 of 0.1 M BR electrolyte was selected for further experiments. Moreover, a linear relationship was observed between varying pH and peak potential and the plot (Fig. 5d) gives a linear regression equation which is  $E_p = -0.0431x + 0.2215$  ( $R^2 = 0.988$ ) and  $E_p = -0.045x + 1.18$  ( $R^2 = 0.985$ ) for AA and LEV respectively. The linear shift of peak potential with pH for AA is  $E_p = -0.0431 \text{ pH} + 0.2215$  ( $R^2 = 0.988$ ) and for LEV is  $E_p =$

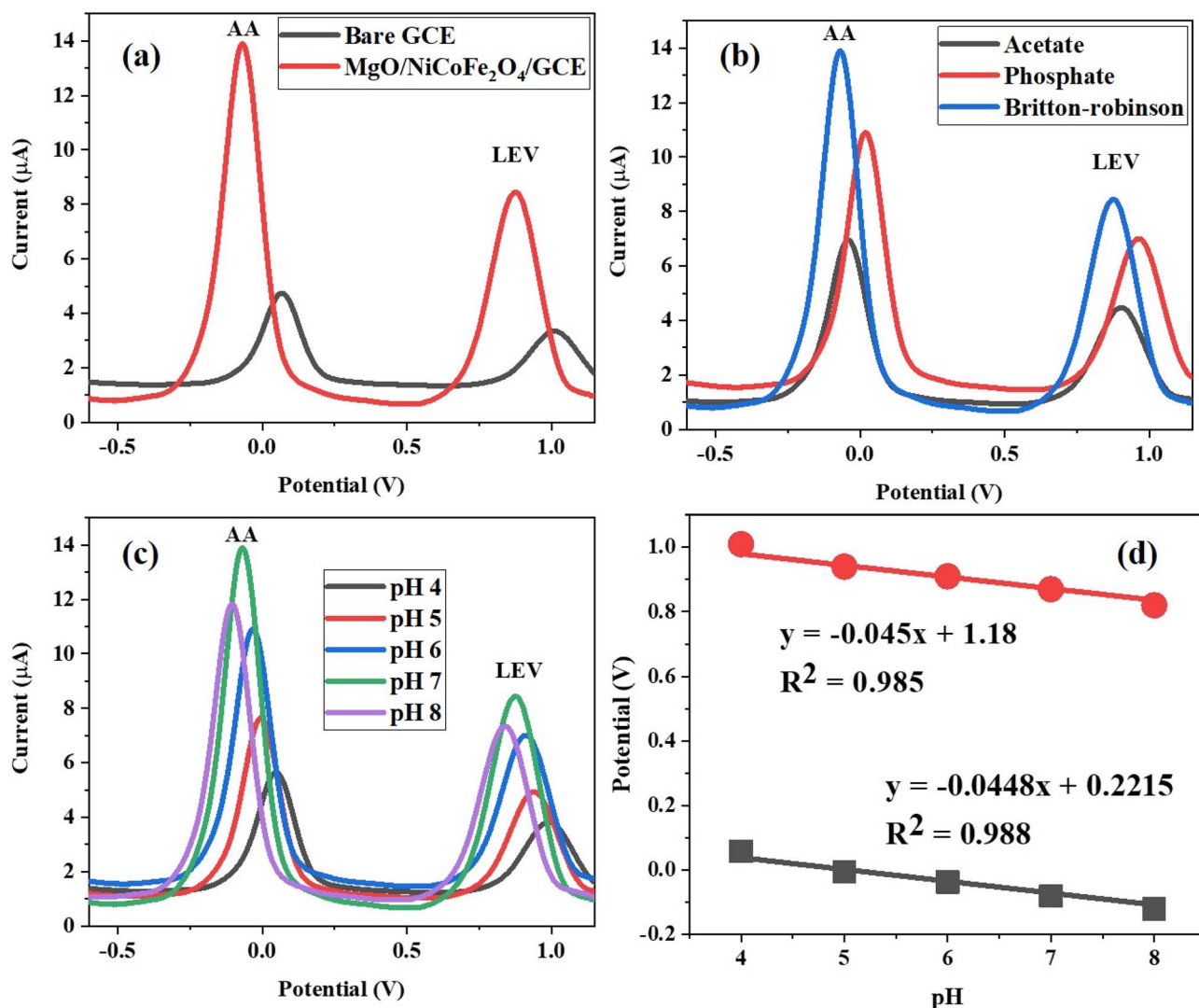


Fig. 5 Optimization study of (a) electrodes, (b) electrolyte, (c) pH and (d) its linear relationship in 250  $\mu\text{M}$  AA and LEV using developed method.



$-0.045 \text{ pH} + 1.18$  ( $R^2 = 0.985$ ). The negative shift of peak potential with increasing pH confirms the participation of protons in the electrode process. According to the Nernst equation, a slope of  $59 \text{ mV pH}^{-1}$  at  $25 \text{ }^\circ\text{C}$  corresponds to an equal number of protons and electrons involved in the redox process. The experimentally obtained slopes ( $\sim 43\text{--}45 \text{ mV pH}^{-1}$ ) are close to the theoretical value, indicating that the oxidation/reduction processes of AA and LEV involve coupled proton-electron transfer reactions.<sup>29</sup> For AA, the electrochemical reaction is attributed to the oxidation of the enediol moiety to dehydroascorbic acid *via* a two-electron/two-proton process, as widely reported in literature. For LEV, oxidation likely occurs at the piperazine nitrogen, leading to *N*-oxide formation *via* a proton-coupled electron transfer mechanism. The pH dependence and electrochemical behavior are consistent with previously reported oxidation pathways of fluoroquinolone antibiotics.<sup>30,31</sup> Further, on this basis, the proposed mechanism for AA and LEV is shown in Scheme 1.<sup>32,33</sup> The proposed mechanisms shown in Scheme 1 are consistent with the observed pH dependence and reported literature.<sup>34</sup>

#### 3.4 Analytical performance of MgO/NiCoFe<sub>2</sub>O<sub>4</sub>-NH/GCE for electrochemical detection of AA and LEV

The calibration plot was drawn between the oxidation current and the concentration of AA and LEV in the range of  $0.05\text{--}400 \text{ } \mu\text{M}$  and  $0.1\text{--}450 \text{ } \mu\text{M}$ , with the regression equations of  $I (\mu\text{A}) = 0.05 \times \text{AA} + 1.027$  and  $I (\mu\text{A}) = 0.027 \times \text{LEV} + 1.043$ , respectively. The coefficient of determination ( $R^2$ ) obtained from the calibration plots indicates strong linearity, with  $R^2$  values of 0.996 and 0.995 (Fig. 6a and b). The limit of detection (LOD) and limit of quantification (LOQ) were calculated using  $3\sigma/\text{slope}$  and  $10\sigma/\text{slope}$ , respectively, where  $\sigma$  is defined as the standard deviation of the calibration residuals, to ensure methodological clarity. The LODs/LOQs of AA and LEV were determined to be  $0.013/0.043$  and  $0.0091/0.03$ , respectively (Akhtar *et al.* 2023).<sup>21</sup> These values indicate competitive sensitivity, though direct comparison with other literature sensors should be interpreted

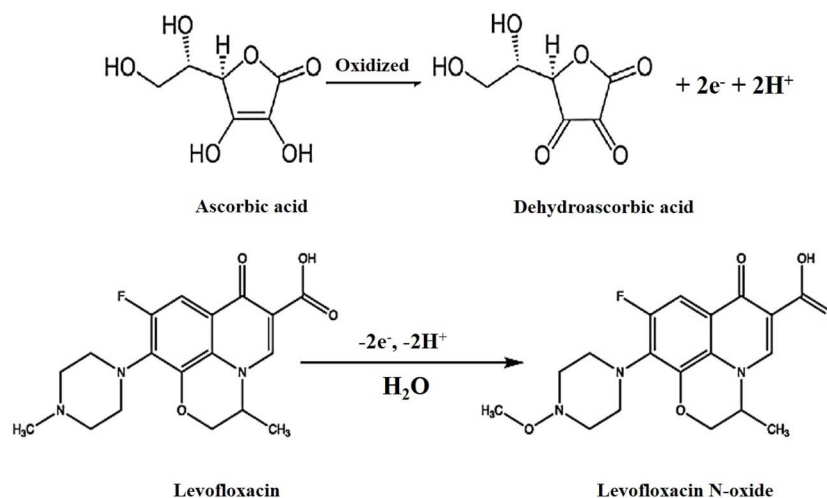
cautiously due to differences in electrode area, technique, and experimental conditions.

The reduction and oxidation peak currents ( $n = 12$ ) of  $250 \text{ } \mu\text{M}$  AA and  $250 \text{ } \mu\text{M}$  LEV were measured using DPV to study the stability of MgO/NiCoFe<sub>2</sub>O<sub>4</sub>-NH/GCE. The results in Fig. 6c indicated the highly stable nature of MgO/NiCoFe<sub>2</sub>O<sub>4</sub>-NH/GCE with % RSD < 2.0 between the peak currents for the electrochemical detection of AA and LEV. Additionally, long-term stability tests were performed by storing the MgO/NiCoFe<sub>2</sub>O<sub>4</sub>-NH/GCE at  $4 \text{ }^\circ\text{C}$  for 30 days and measuring  $250 \text{ } \mu\text{M}$  AA and LEV every 5 days. The peak current retention rate was  $\sim 95\%$ , which represents tolerable stability for potential long-term applications.

To assess the reproducibility of MgO/NiCoFe<sub>2</sub>O<sub>4</sub>-NH/GCE fabrication, three independently prepared MgO/NiCoFe<sub>2</sub>O<sub>4</sub>-NH/GCEs were examined for the detection of  $250 \text{ } \mu\text{M}$  AA and LEV. The obtained current responses were equivalent, with % RSD < 5.0, which demonstrates good reproducibility of the procedure for MgO/NiCoFe<sub>2</sub>O<sub>4</sub>-NH/GCE fabrication.

#### 3.5 Comparative study

The analytical performance of the developed MgO/NiCoFe<sub>2</sub>O<sub>4</sub>-NH-based sensor was compared with previously reported studies (Table 1).<sup>23,28,32,35–37</sup> It is noted that most of the reported sensors focus on the individual detection of either AA or LEV, whereas the proposed MgO/NiCoFe<sub>2</sub>O<sub>4</sub>-NH/GCE enables the simultaneous detection of both analytes in a single measurement step, demonstrating a significant analytical advantage. Further, the developed sensor exhibits a remarkably wide linear dynamic range of  $0.1\text{--}450 \text{ } \mu\text{M}$  for LEV and  $0.05\text{--}400 \text{ } \mu\text{M}$  for AA, which is broader than most previously reported systems. Furthermore, the LODs ( $0.0091 \text{ } \mu\text{M}$  for LEV and  $0.013 \text{ } \mu\text{M}$  for AA) are lower than or comparable to those of earlier studies, demonstrating enhanced sensitivity. The improved analytical performance can be attributed to the synergistic catalytic effect of the MgO/NiCoFe<sub>2</sub>O<sub>4</sub>-NH, which enhances electron transfer kinetics and reduces charge transfer resistance at the electrode



Scheme 1 Reaction mechanism for the oxidation of AA and LEV.



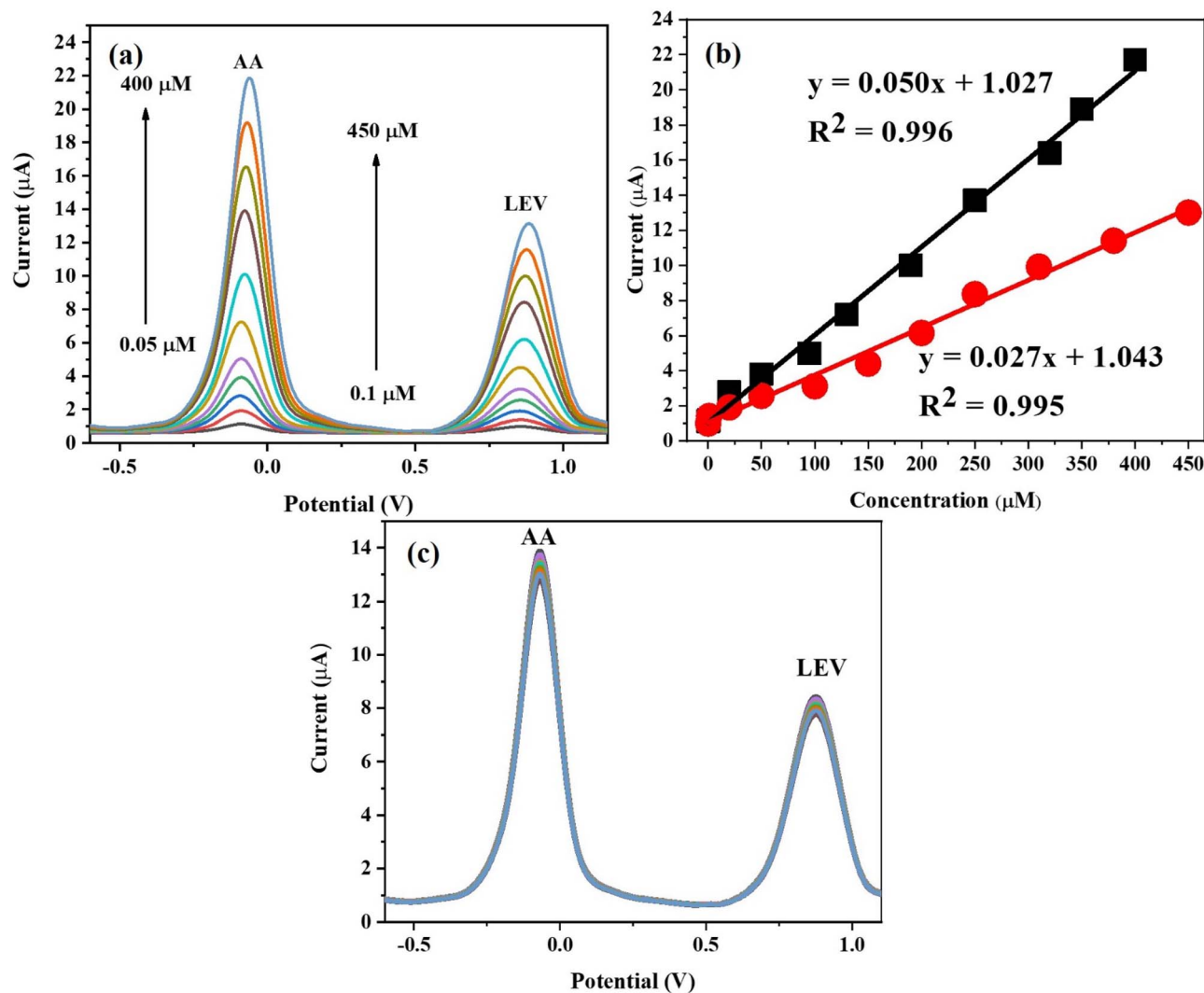


Fig. 6 (a) Calibration, (b) linear relationship of current vs. concentration and (c) stability analysis using MgO/NiCoFe<sub>2</sub>O<sub>4</sub>-NH/GCE-DPV.

Table 1 Comparative study of developed MgO/NiCoFe<sub>2</sub>O<sub>4</sub>-NH/GCE/DPV method with reported studies for the detection of AA and LEV

Material	Technique	Dynamic range (μM)		LOD (μM)		References
		LEV	AA	LEV	AA	
GCE/SnO <sub>2</sub> /MWCNT	DPV	—	1.0–9.9	0.2	—	35
GCE/poly(PGR)	LSV	—	0.5–15	0.097	—	32
GCE/AgNPs-CB-PEDOT:PSS	SWV	—	0.67–12	0.014	—	36
GCE/Gr/Cu	CV	—	0.03–40	0.012	—	28
PAY/MWCNTs/GCE	Amperometry	1–56	—	—	0.2	23
GONR(200 W)/GCE	Amperometry	1.1–8.5	—	—	0.06	37
MgO/NiCoFe <sub>2</sub> O <sub>4</sub> -NH/GCE	DPV	0.1–450	0.05–400	0.0091	0.013	Current study

interface. Moreover, the well-resolved oxidation peaks for AA and LEV allow accurate quantification without mutual interference, which is critical for practical applications involving complex matrices.

Therefore, the proposed sensor not only improves sensitivity and dynamic range but also provides a reliable and efficient

platform for the simultaneous electrochemical determination of AA and LEV, outperforming previously reported methods.

### 3.6 Interference study

The experiments were conducted to assess the reliability of MgO/NiCoFe<sub>2</sub>O<sub>4</sub>-NH/GCE to guarantee precise detection in



**Table 2** Interference study of numerous species for the detection of 250  $\mu\text{M}$  ascorbic acid and levofloxacin by  $\text{MgO}/\text{NiCoFe}_2\text{O}_4\text{-NH}/\text{GCE}$ 

Interfering species	Recovery (%)	Relative standard deviation (%)
Casein	96.5	0.99
Lactose	95.13	1.71
Dopamine	97.83	1.67
Glucose	96.7	1.65
Paracetamol	98.6	0.94
Uric acid	97.82	0.92
Ciprofloxacin	95.87	1.78
$\text{Pb}^{2+}$	97.54	1.69
$\text{Ca}^{2+}$	97.69	1.72
$\text{Mg}^{2+}$	97.26	1.65

addition to target analyte determination and differentiate against possible interfering substances.<sup>38</sup> Using DPV, a variety of interfering substances were examined at concentrations 100 times higher than the analyte (AA and LEV), including casein (CA), lactose (LA), dopamine (DP), glucose (GU), paracetamol (PA), uric acid (UA), ciprofloxacin (CP), and other metal ions such as lead ( $\text{Pb}^{2+}$ ), calcium ( $\text{Ca}^{2+}$ ), and magnesium ( $\text{Mg}^{2+}$ ). Research reveals that a small number of selected species have little interference with  $\text{MgO}/\text{NiCoFe}_2\text{O}_4\text{-NH}/\text{GCE}$ , with a percentage RSD of 1.78. While these results indicate good preliminary selectivity, the fixed 100-fold excess does not fully replicate the variability of real sample matrices. Future studies involving concentration-dependent interference and mixed-interferent systems are necessary to evaluate sensor performance under more realistic conditions. This suggests that  $\text{MgO}/\text{NiCoFe}_2\text{O}_4\text{-NH}/\text{GCE}$  functions very well for AA and LEV sensing in the presence of various sample media (Table 2), but caution should be taken when extrapolating these results to complex, real-world samples.

### 3.7 Real sample study

The developed  $\text{MgO}/\text{NiCoFe}_2\text{O}_4\text{-NH}/\text{GCE}/\text{DPV}$  method was applied to detect AA and LEV in blood, dairy milk (cow, buffalo, and cattle), and wastewater (Table 3). These matrices were selected to represent biologically and environmentally relevant samples with varying complexity and potential interfering components. The concentration of AA and LEV in blood and dairy milk was found below the detection limit (BDL) by application of the developed method. The absence of detectable native levels in these samples suggests either low environmental prevalence or concentrations below the sensitivity limit of the present method under the tested conditions. The reliability of the developed  $\text{MgO}/\text{NiCoFe}_2\text{O}_4\text{-NH}/\text{GCE}/\text{DPV}$  method was evaluated for the detection of AA and LEV using the standard addition method. The blood samples were analyzed by spiking known concentrations of AA and LEV (20, 50, and 100  $\mu\text{M}$ ), and the obtained amounts were calculated. The concentration of AA ranged from 97.6–100.3% with a RSD of less than 1.2%, and the concentration of LEV ranged from 98.4–100.3% with a RSD of less than 1.0% by applying the standard addition method. These high recovery values with low RSD confirm good

**Table 3** Determination and validation of AA and LEV in blood, dairy milk (cow, buffalo, and cattle), and wastewater ( $n = 3$ ) using  $\text{MgO}/\text{NiCoFe}_2\text{O}_4\text{-NH}/\text{GCE}$ 

Sample	Added ( $\mu\text{M}$ )	Conc. ( $\mu\text{M}$ )	Recovery (%)	RSD (%)
<b>Ascorbic acid</b>				
Blood	0	BDL	—	—
	20	$19.7 \pm 0.22$	97.6–99.8	1.14
	50	$49.8 \pm 0.28$	99.0–100.2	0.56
	100	$99.9 \pm 0.42$	99.5–100.3	0.42
Dairy milk	0	BDL	—	—
	10	$9.79 \pm 0.25$	95.4–100.4	2.55
	20	$19.9 \pm 0.34$	97.8–101.2	1.71
	30	$29.9 \pm 0.39$	98.5–101.1	1.30
Waste water	0	BDL	—	—
	10	$9.8 \pm 0.12$	96.8–99.2	1.22
	20	$19.4 \pm 0.25$	95.7–98.2	1.28
	30	$29.87 \pm 0.4$	98.2–100.9	1.34
<b>Levofloxacin</b>				
Blood	0	BDL	—	—
	20	$19.85 \pm 0.18$	98.4–100.2	0.90
	50	$49.86 \pm 0.26$	99.2–100.24	0.52
	100	$99.94 \pm 0.38$	99.6–100.3	0.38
Dairy milk	0	BDL	—	—
	10	$9.73 \pm 0.22$	95.1–99.5	2.26
	20	$19.8 \pm 0.24$	97.9–100.3	1.21
	30	$29.89 \pm 0.32$	98.6–100.7	1.07
Waste water	0	BDL	—	—
	10	$9.68 \pm 0.18$	95.0–98.6	1.85
	20	$19.74 \pm 0.23$	97.45–99.95	1.13
	30	$29.83 \pm 0.38$	98.16–100.7	1.27

accuracy, precision, and minimal matrix interference in blood samples.

Further, the prepared dairy milk samples were analyzed by spiking known concentrations of AA and LEV (10, 20 and 30  $\mu\text{M}$ ), and the obtained amounts were calculated. The concentration of AA ranged from 95.4–101.2% with a RSD of less than 2.6%, and the concentration of LEV ranged from 95.1–100.7% with a RSD of less than 2.3% by applying the standard addition method. The satisfactory recoveries in milk samples demonstrate acceptable matrix compatibility despite the presence of proteins, fats, and other organic constituents.

Moreover, the results indicated that 0.097 and 0.043  $\mu\text{M}$  of AA and LEV were found in industrial effluents, respectively. The detection of measurable concentrations in industrial effluent samples indicates potential environmental relevance of the developed method. The AA and LEV were found below the detection limit (BDL) in tap water samples. This may reflect effective water treatment processes or concentrations lower than the detection capability of the current analytical system.

The tap water and industrial effluents were analyzed by spiking known concentrations of AA and LEV (10, 20, and 30  $\mu\text{M}$ ), and the obtained amounts were calculated. The concentration of AA and LEV ranged from 96.3–103.1% and a percentage RSD of less than 2.0% by applying the standard addition method. These results primarily validate the analytical accuracy and robustness of the method in complex aqueous matrices rather than indicating widespread contamination.



These results indicate the high reliability and accuracy of the MgO/NiCoFe<sub>2</sub>O<sub>4</sub>-NH/GCE-based electroanalytical method for determining AA and LEV in wastewater samples. However, broader environmental monitoring studies and evaluation under mixed-interferent conditions would further strengthen the demonstration of field applicability.

## 4 Conclusion

In this work, a MgO-modified nickel-cobalt ferrite nanohybrid (MgO/NiCoFe<sub>2</sub>O<sub>4</sub>-NH) was successfully synthesized *via* a green-assisted route and employed for the simultaneous electrochemical detection of AA and LEV. Structural analysis confirmed the formation of a spinel-type NiCoFe<sub>2</sub>O<sub>4</sub> phase, while MgO incorporation influenced crystallite size and surface morphology. Although the hybrid material exhibited preserved crystallinity, the coexistence of MgO and ferrite phases indicates a composite system rather than a strictly single-phase structure. Further, the electrochemical investigations demonstrated enhanced current response and improved peak separation compared to the unmodified electrode. The improved performance is attributed to the synergistic interaction between MgO and NiCoFe<sub>2</sub>O<sub>4</sub>, which likely facilitates charge transport and increases the density of electroactive sites. However, direct kinetic parameters were not comprehensively quantified, and therefore, the enhancement in electron-transfer kinetics is inferred primarily from voltammetric behavior. Moreover, the developed MgO/NiCoFe<sub>2</sub>O<sub>4</sub>-NH/GCE showed good sensitivity, repeatability, and selectivity in buffer solutions and spiked real samples (serum, milk, and wastewater). While these results demonstrate promising analytical capability, the validation was conducted using fortified samples rather than authentic clinical or pharmaceutical formulations at native concentrations. Therefore, further studies involving certified reference materials, broader interference studies, long-term stability assessment, and full electrochemical impedance analysis are required before practical utilization in pharmaceutical quality control or clinical diagnostics can be claimed.

## Ethical statement

This study was conducted with the informed consent of the selected healthy volunteer participants, who provided biological samples for the electrochemical determination of AA and LEV. The selected participants were fully informed of the purpose of the study, utilized procedures, the possible risks, and the predicted benefits, and were assured of the confidentiality and anonymity of their data. An ethical board is not established for ethical standards-based approval for research involving human subjects. However, the study procedure was designed according to the agreement recommended in the Helsinki declaration.

## Author contributions

The current study is a result of the visionary work of Dr Jameel Ahmed Baig, Prof. Dr Imam Bakhsh Solangi, and Dr Huma Shaikh, who provided their contribution as supervision, project

management, review, and editing. Mr Latif Ullah Khan, Dr Sajjad Hussain, Prof. Dr Faisal K. Algethami, and Prof. Dr Nadeem Raza provided their assistance for the characterization of material, interpretation, and evaluation. A committed PhD student, Ms Iram Gul, played a pivotal role in the creation of the original draft, its formal analysis, data curation, and methodology. Dr Saima Perveen expertly managed the technical aspects, including software use, research, and visualization.

## Conflicts of interest

The authors state that none of the work presented in this study was influenced by any known conflicting financial interests or personal ties.

## Data availability

Access to the data assisting with the current research project can be granted upon formal request.

Supplementary information (SI) is available. See DOI: <https://doi.org/10.1039/d6ra00424e>.

## Acknowledgements

This work was supported and funded by the Deanship of Scientific Research at Imam Mohammad Ibn Saud Islamic University (IMSIU) (grant number IMSIU-DDRSP2602).

## References

- 1 K. Kümmerer, The presence of pharmaceuticals in the environment due to human use—present knowledge and future challenges, *J. Environ. Manage.*, 2009, **90**(8), 2354–2366.
- 2 J. A. Baig, Advanced approach of magnetic nanohybrids in removal of pharmaceutical based pollutants, in *Functionalized Magnetic Nanohybrids*, Elsevier, 2025, pp. 285–328.
- 3 P. Vaudin, C. Augé, N. Just, S. Mhaouty-Kodja, S. Mortaud and D. Pillon, When pharmaceutical drugs become environmental pollutants: Potential neural effects and underlying mechanisms, *Environ. Res.*, 2022, **205**, 112495.
- 4 S. K. Khetan and T. J. Collins, Human pharmaceuticals in the aquatic environment: a challenge to green chemistry, *Chem. Rev.*, 2007, **107**(6), 2319–2364.
- 5 H. Brohi, T. G. Kazi, H. I. Afridi, F. K. Algethami, J. A. Baig and A. Unar, Comparative analysis of electrolyte and essential trace elemental contents in cow and buffalo's raw milk versus processed/pasteurized milk: Implications for estimated daily intake, *J. Food Compos. Anal.*, 2026, **151**, 108977.
- 6 I. T. Khan, M. Bule, R. Ullah, M. Nadeem, S. Asif and K. Niaz, The antioxidant components of milk and their role in processing, ripening, and storage: Functional food, *Vet. World*, 2019, **12**(1), 12.



- 7 S. Sachi, J. Ferdous, M. H. Sikder and S. A. K. Hussani, Antibiotic residues in milk: Past, present, and future, *J. Adv. Vet. Anim. Res.*, 2019, **6**(3), 315.
- 8 J. R. Shaikh and M. Patil, Drug residues in milk and milk products: sources, public health impact, prevention and control, *Int. J. Livest. Res.*, 2020, **10**, 24–36.
- 9 M. M. J. Arsène, A. K. L. Davares, P. I. Viktorovna, S. L. Andreevna, S. Sarra, I. Khelifi and D. M. Sergueïevna, The public health issue of antibiotic residues in food and feed: Causes, consequences, and potential solutions, *Vet. World*, 2022, **15**(3), 662–671.
- 10 S. O. Fakayode, C. Lisse, W. Medawala, P. N. Brady, D. K. Bwambok, D. Anum, T. Alonge, M. E. Taylor, G. A. Baker, T. F. Mehari and J. D. Rodriguez, Fluorescent chemical sensors: applications in analytical, environmental, forensic, pharmaceutical, biological, and biomedical sample measurement, and clinical diagnosis, *Appl. Spectrosc. Rev.*, 2024, **59**(1), 1–89.
- 11 S. K. Patial and S. Singh, Sensors for the Detection of Pharmaceuticals in Wastewater and Natural Waters, *Reference Module in Chemistry, Molecular Sciences and Chemical Engineering*, Elsevier, 2024.
- 12 M. Ashiq, Structural, dielectric, morphological and magnetic properties of cobalt-substituted nickel spinel ferrites (CoxNi1-xFe2O4) nanoparticles, *Appl. Nanosci.*, 2023, **13**(6), 4541–4554.
- 13 Y. Krishnan, K. Babu, S. Sakkaraiyan, A. Dinesh, A. Shanmugam, K. Radhakrishnan and M. Ayyar, Spinel cobalt ferrite nanoparticles for photocatalysts, sensor and biomedical applications: a review, *Semiconductors*, 2024, **58**(9), 721–739.
- 14 L. Zuo, H. Yang, H. Li, Y. Zhang, L. Gao, Y. Zhang and F. Wang, Magneto-Photo Synergism Enhances Oxygen Evolution Reaction on Hollow NiCo<sub>2</sub>O<sub>4</sub> Microboxes, *Adv. Funct. Mater.*, 2026, **36**(15), e19261.
- 15 S. Perveen, J. A. Baig, S. T. H. Sherazi, S. Memon, K. Akhtar, S. Hussain and F. Abbasi, Green synthesis of electroactive magnesium ferrite nanoparticles for the selective determination of mefenamic acid in blood, pharmaceutical products, and wastewater, *Anal. Lett.*, 2025, **58**(14), 2395–2410.
- 16 Z. Ali, J. A. Baig, H. I. Afridi, K. Akhtar, S. Perveen and N. Raza, Simultaneous electrochemical detection of Cu, Cd and Mn by nickel ferrite-cobalt ferrite bimetallic nanocomposite, *RSC Adv.*, 2025, **15**(58), 50470–50480.
- 17 S. Hussain, I. Chandio, M. A. Rashid, I. Sadiq, J. A. Baig, S. A. Solangi, M. Shahbaz and K. H. Thebo, Synthesis of Nano-ferrites-based Materials: A New Paradigm for Electrochemical Sensors, *J. Environ. Chem. Eng.*, 2025, **13**(6), 120218.
- 18 M. Khan, J. A. Baig, F. N. Talpur, S. Perveen, H. I. Afridi, K. Akhtar and N. Raza, Alginate-coated cobalt ferrite nanocomposite for preconcentration of heavy metals using dispersive solid phase extraction, *RSC Adv.*, 2026, **16**(14), 12265–12274.
- 19 X. Kong, *et al.*, NiO load K<sub>2</sub>Fe<sub>4</sub>O<sub>7</sub> enhanced photocatalytic hydrogen production and photo-generated carrier behavior, *J. Alloys Compd.*, 2022, **903**, 163864.
- 20 M. Ma, T. Zhe, Y. Ma, Z. Wang, Q. Chen and J. Wang, Highly sensitive and reproducible non-enzymatic glucose sensor fabricated by drop-casting novel nanocomposite with 3D architecture and tailorable properties prepared in controllable way, *Talanta*, 2018, **180**, 133–143.
- 21 K. Akhtar, *et al.*, Biosynthesis and characterization of NiFe<sub>2</sub>O<sub>4</sub>-NPs for electrochemical detection of ceftriaxone from biological and pharmaceutical samples, *Microchem. J.*, 2023, **191**, 108808.
- 22 G. Datt, M. S. Bishwas, M. M. Raja and A. Abhyankar, Observation of magnetic anomalies in one-step solvothermally synthesized nickel-cobalt ferrite nanoparticles, *Nanoscale*, 2016, **8**(9), 5200–5213.
- 23 S. A. Kumar, S.-F. Wang, T. C.-K. Yang and C.-T. Yeh, Acid yellow 9 as a dispersing agent for carbon nanotubes: Preparation of redox polymer-carbon nanotube composite film and its sensing application towards ascorbic acid and dopamine, *Biosens. Bioelectron.*, 2010, **25**(12), 2592–2597.
- 24 K. Akhtar, F. K. Algethami, J. A. Baig, I. B. Solangi, H. I. Afridi, L. U. Khan, Y. G. Abou El-Reash and S. Hussain, Synthesis of cobalt-doped nickel ferrite as a reusable photocatalyst for efficient degradation of industrial dyes, *Mater. Res. Bull.*, 2025, **195**, 113830.
- 25 D. Koningsberger, B. Mojet, G. Van Dorssen and D. Ramaker, XAFS spectroscopy; fundamental principles and data analysis, *Top. Catal.*, 2000, **10**, 143–155.
- 26 M. Hayat, A. Shah, J. Nisar, I. Shah, A. Haleem and M. N. Ashiq, A novel electrochemical sensing platform for the sensitive detection and degradation monitoring of methylene blue, *Catalysts*, 2022, **12**(3), 306.
- 27 Q. Wang, M. Yang, X. Qi, J. Wang, K. Sun, Z. Li and G. Deng, A novel graphene oxide decorated with halloysite nanotubes (HNTs/GO) composite used for the removal of levofloxacin and ciprofloxacin in a wide pH range, *New J. Chem.*, 2021, **45**(39), 18315–18326.
- 28 T. Yu, P. R. Kasturi and C. B. Breslin, Ultra-sensitive electrochemical detection of levofloxacin using a binder-free copper and graphene composite, *Talanta*, 2024, **275**, 126132.
- 29 A. M. Pisoschi, A. Pop, A. I. Serban and C. Fafaneata, Electrochemical methods for ascorbic acid determination, *Electrochim. Acta*, 2014, **121**, 443–460.
- 30 S. Tursynbolat, Y. Bakytkarim, J. Huang and L. Wang, Ultrasensitive electrochemical determination of metronidazole based on polydopamine/carboxylic multi-walled carbon nanotubes nanocomposites modified GCE, *J. Pharm. Anal.*, 2018, **8**(2), 124–130.
- 31 X. Zhao, *et al.*, Fe-Decorated nitrogen-doped carbon nanospheres as an electrochemical sensing platform for the detection of acetaminophen, *Molecules*, 2023, **28**(7), 3006.
- 32 Ç. C. Koçak, B. Aşlışen, Ş. Karabiberoglu, K. V. Özdokur, A. Aslan and S. Koçak, Electrochemical determination of



- levofloxacin using poly (pyrogallol red) modified glassy carbon electrode, *ChemistrySelect*, 2022, 7(41), e202201864.
- 33 Y. Kim and M.-G. Kim, HPLC-UV method for the simultaneous determinations of ascorbic acid and dehydroascorbic acid in human plasma, *Transl. Clin. Pharmacol.*, 2016, 24(1), 37–42.
- 34 S. Arya, M. Mahajan and P. Jain, Non-spectrophotometric methods for the determination of Vitamin C, *Anal. Chim. Acta*, 2000, 417(1), 1–14.
- 35 V. Cesarino, I. Cesarino, F. C. Moraes, S. A. Machado and L. H. Mascaro, Carbon nanotubes modified with SnO<sub>2</sub> rods for levofloxacin detection, *J. Braz. Chem. Soc.*, 2014, 25, 502–508.
- 36 A. Wong, A. M. Santos and O. Fatibello-Filho, Simultaneous determination of paracetamol and levofloxacin using a glassy carbon electrode modified with carbon black, silver nanoparticles and PEDOT: PSS film, *Sens. Actuators, B*, 2018, 255, 2264–2273.
- 37 C. L. Sun, C. T. Chang, H. H. Lee, J. Zhou, J. Wang, T. K. Sham and W. F. Pong, Microwave-assisted synthesis of a core-shell MWCNT/GONR heterostructure for the electrochemical detection of ascorbic acid, dopamine, and uric acid, *ACS Nano*, 2011, 5(10), 7788–7795.
- 38 X. Xie, D. P. Wang, C. Guo, Y. Liu, Q. Rao, F. Lou, Q. Li, Y. Dong, Q. Li, H. B. Yang and F. X. Hu, Single-atom ruthenium biomimetic enzyme for simultaneous electrochemical detection of dopamine and uric acid, *Anal. Chem.*, 2021, 93(11), 4916–4923.

